# Mechanics of Biohybrid Valveless Pump-Bot

# Zhengwei Li

Department of Mechanical Science and Engineering, University of Illinois at Urbana-Champaign, Urbana, IL 61801 e-mail: zhengwei@illinois.edu

# M. Taher A. Saif<sup>1</sup>

Department of Mechanical Science and Engineering, University of Illinois at Urbana-Champaign, Urbana, IL 61801 e-mail: saif@illinois.edu

Engineering living systems is a rapidly emerging discipline where the functional biohybrid robotics (or "Bio-bots") are built by integrating of living cells with engineered scaffolds. Inspired by embryonic heart, we presented earlier the first example of a biohybrid valveless pump-bot, an impedance pump, capable of transporting fluids powered by engineered living muscle tissues. The pump consists of a soft tube attached to rigid boundaries at the ends, and a muscle ring that squeezes the tube cyclically at an off-center location. Cyclic contraction results in a net flow through the tube. We observed that muscle force occasionally buckles the tube in a random fashion, i.e., similar muscles do not buckle the tube consistently. In order to explain this anomaly, here we develop an analytical model to predict the deformation and stability of circular elastic tubes subjected to a uniform squeezing force due to a muscle ring (like a taught rubber band). The prediction from the model is validated by comparing with experiments and finite element analysis. The nonlinear model reveals that the circular elastic tube cannot buckle irrespective of muscle force. Buckling state can be reached and sustained by bending and folding the tube before applying the muscle ring. This imperfection may appear during assembly of the pump or from nonuniform thickness of the muscle ring. This study provides design guides for developing advanced biohybrid impedance pumps for diverse applications.

[DOI: 10.1115/1.4051595]

Keywords: biohybrid robotics, pump-bot, mechanics modeling, buckling

#### 1 Introduction

Biohybrid robotics consisting of living cells and biomaterials have recently attracted great interests for diverse scientific research and technological applications over the past decade [1–5]. Due to the integration with living components, bio-bots have shown promising outcomes and unprecedented properties, such as self-healing, self-assembling, and dynamic sensing, responding, and adapting to the environmental cues in real time [6,7]. In addition, the biohybrid systems are biocompatible and can be operated noninvasively by electrical, optical, or chemical signals without the need for large-scale external driving systems, which makes them favorable for a wide range of biomedical applications [3]. Furthermore, the biohybrid design strategy provides the potential to construct more complex bio-integrated machines or systems with unprecedented performances at the macroscale and to enable the development of self-powered autonomous microrobots [2].

Pioneering studies have used muscle cells or tissue constructs for actuation for walking [7–9], swimming [10–12], gripping [13–15], and pumping [16-18] bio-bots. For example, Chan et al. [8] developed a biohybrid walker by integrating 3D-printed hydrogel structure with an engineered muscle stripe. Here, cyclic contraction of muscle tissue deforms an asymmetric structure for walking, where the speed was controlled by applying the electrical stimulation frequencies. Park et al. [10] created a biohybrid robotic stingray powered by optogenetic heart cells. The swimming speed and direction was controlled by modulating light stimulation frequency and position. Williams et al. [11] built a self-powered biohybrid swimmer by combining a thin PDMS filament with cardiomyocytes, where the cardiomyocytes contract and deform the filament to propel the swimmer. Morimoto et al. [13] built a biohybrid gripper by assembling an antagonistic pair of skeletal muscle tissues with a soft robotic that can mimic the actions of human

finger. Currently, the majority of developed bio-bots are motile bots which utilize the contraction of living muscle cells or tissues to achieve the desired locomotion.

Inspired by the early embryonic heart, we developed a new type of bio-bot (i.e., "Pump-bot") with the ability to transport fluid through a synthetic conduit, powered by engineered skeletal muscle in a spontaneous or electric-responsive manner [16]. Such living muscle-driven pumps may have significant impact and broad utility in wide range of biomedical applications in microfluidics, drug delivery, biomedical implants, and cardiovascular pumping system. Figure 1(a-i) shows the conceptual design of pump-bot which utilizes the impedance-based pumping mechanism for valveless pumping. It consists of a soft hydrogel tube connected at both ends to a rigid tube, creating an impedance mismatch, and a tissue-engineered muscle ring wrapping around the soft tube at an off-center position for the pumping action. Cyclic muscle contractions along the circumferential direction, spontaneous or electrically stimulated, induces radial compression of the soft tube (Fig. 1(a-ii)), resulting in elastic waves that propagate along the soft tube and get reflected back at the soft/stiff tube boundaries. Asymmetric placement of muscle ring results in a time delay between the wave arrivals. This dynamic wave interaction establishes a pressure gradient between the two ends of soft hydrogel tube, resulting in a net unidirectional flow. To construct the pump-bot, skeletal muscle rings are first formed by seeding the mixture of mouse skeletal myoblasts with collagen I and matrigel onto the circular silicone molds. Upon polymerization, the cell-laden gel is compacted by cellular traction forces resulting in a muscle ring (Fig. 1(b-i)). Then, ring is transferred onto a hydrogel tube with the outer diameter of 4 mm, wall thickness of 0.2 mm, and elastic modulus of 10 kPa (Fig. 1(b-ii)). Next, the hydrogel tube-muscle ring assembly is inserted into a PDMS fluidic platform to complete the pump-bot circuit (Fig. 1(b-iii)). Impressive high flowrates (up to  $22.5 \mu L/min$ ) are achieved, which are at least three orders of magnitude higher than those from previous reported cardiomyocyte powered biohybrid valve pumps of similar size [17,18].

To develop more complex pump-bots, we need to fully understand the underlying mechanics that emerge at the interface of muscle tissues and synthetic conduits [19,20], which guide the

<sup>&</sup>lt;sup>1</sup>Corresponding author.

Contributed by the Applied Mechanics Division of ASME for publication in the JOURNAL OF APPLIED MECHANICS. Manuscript received June 11, 2021; final manuscript received June 21, 2021; published online July 12, 2021. Assoc. Editor: Yonggang Huang.

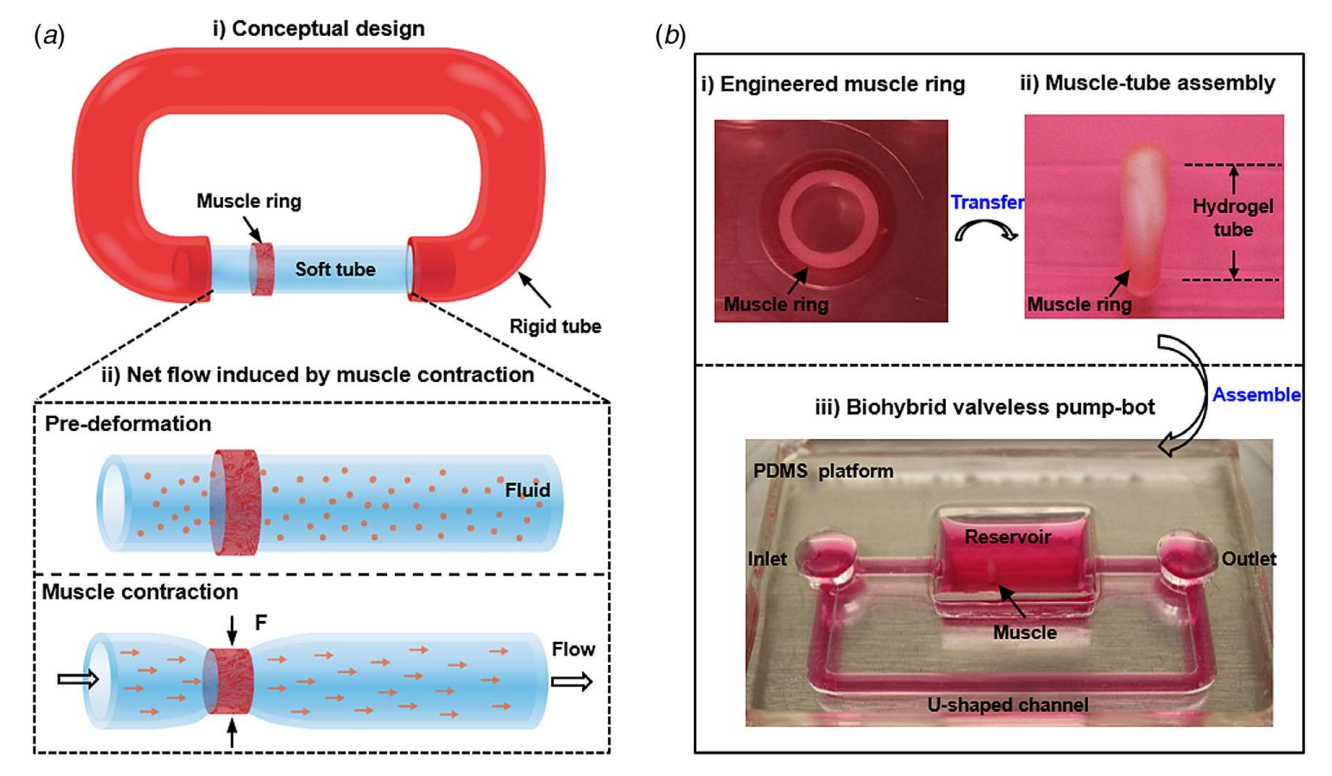


Fig. 1 (a) The proposed conceptual design of biohybrid valveless pump-bot, which consists of a soft tube connected at both ends to a rigid tube with an engineered muscle ring wrapping around the soft tube at an off-center location, forming an impedance pump. (b) The fabrication and assembly of pump-bot. The skeletal muscle ring (i) fabricated from the silicone molds is first transferred to the hydrogel tube (ii), then hydrogel tube-muscle ring assembly is connected to the PDMS fluidic platform to enable a biohybrid valveless pump-bot (iii).

design and optimization of such biohybrid system. After assembly (Fig. 1(b-iii)), the pump-bot is incubated in the muscle differentiation medium to induce formation of contractile myotubes within the muscle tissue. The muscle ring with myotubes applies a contractile force, T, on the elastic hydrogel tube as a taut rubber band on a tube segment. During the static muscle contraction process, some hydrogel tubes show significant reduction in diameter and buckling/ folding while others do not, even though the muscle ring are nominally similar, and the tubes are made similarly. In this work, we first established an analytical mechanics model to calculate the muscle tension force based on the tube deformation, which are further validated by comparing with both the experiment and finite element analysis. Furthermore, we performed the buckling and postbuckling analysis to explain the buckling or folding phenomenon observed in the development of some pump-bots and obtained the total free energy of whole pumping system under the various static muscle contraction forces. The results show that the buckling of hydrogel tube is facilitated by nonuniformity of the muscle force and geometry and/or the nonuniformity of the tube thickness along the circumferential direction. This study provides important insights into the design and fabrication of nextgeneration bio-integrated machines and systems for a broad range of biomedical applications.

#### 2 Muscle Tension Force Calculation

**2.1 Analytical Model.** In the experiment, the muscle ring shrinks over time and applies a radial compression on the hydrogel tube. Consequently, the tube radius decreases elastically. Due to the resistance of the tube, the muscle becomes subjected to tension. An analytical model is established to estimate the muscle tension from the measured decrease of tube radius as shown in Fig. 2(a). Consider an elastic tube with thickness t and radius t (at the mid thickness). The elastic modulus of the tube material is t. The muscle ring, of width t0, applies a contractile force on the tube. Thus, the

muscle spans a length, w, of the tube. The length of the tube is much larger than w. Let T be the tension in the muscle, and y be the corresponding decrease in the radius of the tube due to tension T. Within the width of the muscle,  $y = y_0$ . Let x be the coordinate along the length of the tube with x = 0 at the edge of the muscle

We want to develop an analytical model relating T and  $y_0$ ,  $T = T(y_0)$ . We can estimate the muscle tension from measured deformation,  $y_0$ , of the tube. We solve the problem in two steps: (1) quantify the tension,  $T_1$ , required to deform (reduce diameter) an isolated segment of the tube of length w by  $y_0$  (Fig. 2(b)), and (2) quantify the tension,  $T_2$ , required to deform the rest of the tube by y(x) (Fig.  $y_0$ ). Step (1) involves circumferential compression of the tube only. Step (2) involves both circumferential compression and longitudinal bending of the tube. The net tension in the muscle is the sum of the tension in steps (1) and (2),  $T = T_1 + T_2$ . For step (1), tension,  $T_1$  is given by the force balance:

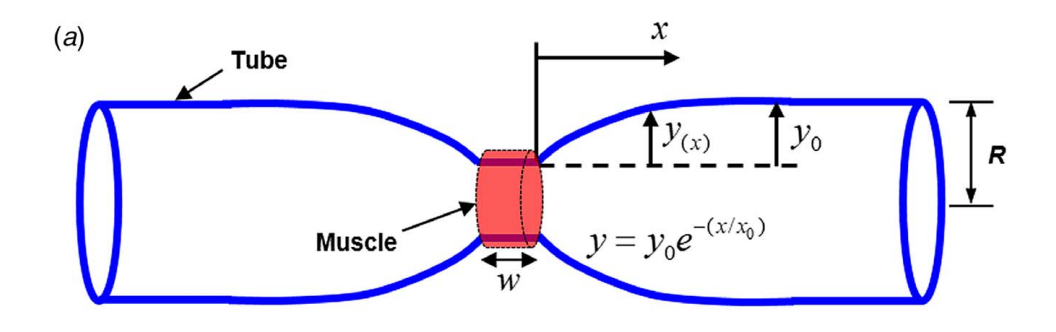
$$T_1 = wtE_t \frac{y_0}{R} \tag{1}$$

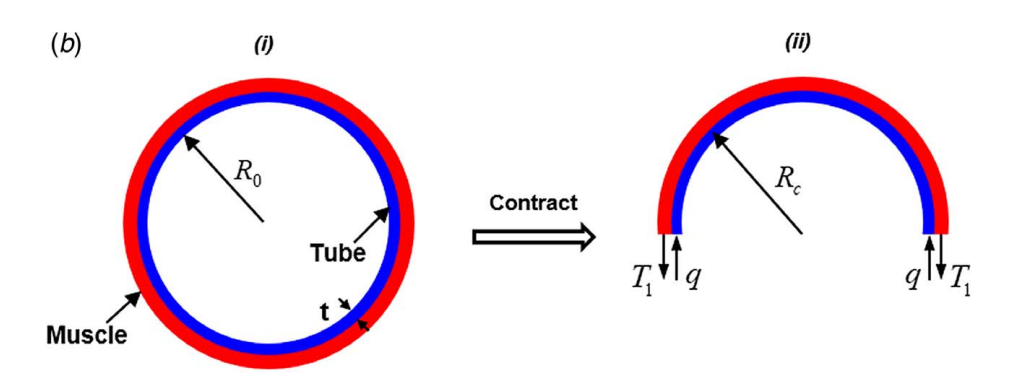
For step (2), we evaluate the strain energy associated with circumferential compression,  $U_c$  and bending,  $U_b$ . Consider a small length, dx, of the tube at distance x from the string. The tube radius decreases by y at x, where  $y(x=0)=y_0$ . Thus, the perimeter of the tube at x decreases by  $2\pi y$ . Then the strain energy due to the circumferential compression can be expressed as

$$U_c = \int \sigma \varepsilon(x) (2\pi R - 2\pi y) \frac{t dx}{2}$$
 (2)

where  $\varepsilon(x) = y/R$  and  $\sigma = E_r \varepsilon$ . Since  $y/R \ll 1$ , the above equation can be further simplified as

$$U_c = \frac{\pi E_t t}{R} \int_0^\infty y^2 dx \tag{3}$$





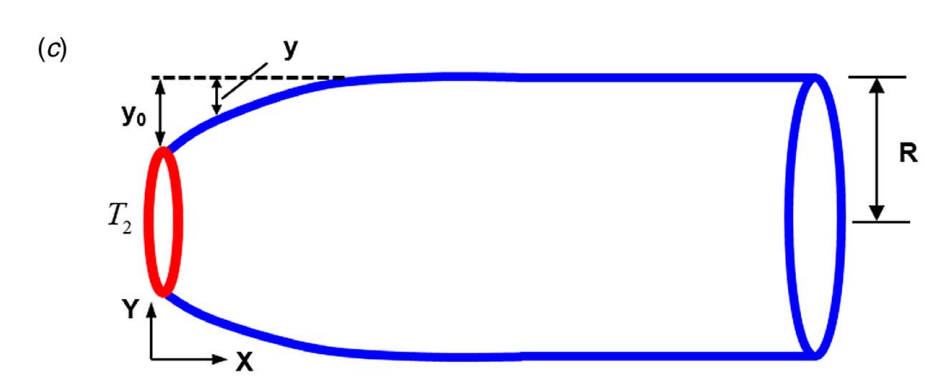


Fig. 2 (a) A full analytical model is established to estimate the muscle tension force from the measured decrease of tube radius. (b) The cross-sectional view of an isolated segment of the tube of length w to quantify the tension  $T_1$ . (c) The part of analytical model to determine the tension  $T_2$  required to deform the rest of the tube.

(5)

Bending energy can be expressed as

$$U_b = \frac{\pi E_t R t^3}{12} \int y''^2 dx \tag{4}$$

So, the total energy can be obtained as

$$U_{total} = \frac{\pi E_t R t^3}{12} \int y'^2 dx + \frac{\pi E_t t}{R} \int y^2 dx$$

Work done by the muscle is

$$W = 2\pi \int_{0}^{y_0} T_2 y dy \tag{6}$$

Conservation of energy results in  $W=2(U_b+U_c)$ , where the factor 2 accounts for the energy on both sides of the muscle ring. Then

$$T_2 = \frac{2E_t t}{y_0} \left[ \frac{1}{R} \int_0^\infty y^2 dx + \frac{Rt^2}{12} \int_0^\infty y''^2 dx \right]$$
 (7)

For simplicity, let  $y = y_0 e^{-x/x_0}$ , where  $x_0$  is a characteristic length scale.  $x_0$  is obtained from the principle of minimum potential energy, i.e., from  $dU_{total}/dx_0 = 0$ 

$$x_0 = \sqrt{\frac{Rt}{2}} \tag{8}$$

Therefore, for the muscle ring with width w, the total tension force can be obtained by

$$T = T_1 + T_2 = y_0 \left( t E_t \frac{w}{R} + t E_t \sqrt{\frac{2t}{R}} \right)$$
 (9)

This gives analytically the relationship between the muscle tension T and the static contraction amounty<sub>0</sub>.

**2.2 Experimental Comparison.** To verify the assumption on the tube deformation profile,  $y = y_0 e^{-x/x_0}$ , we compared the exponential expression with the experimental measurements.

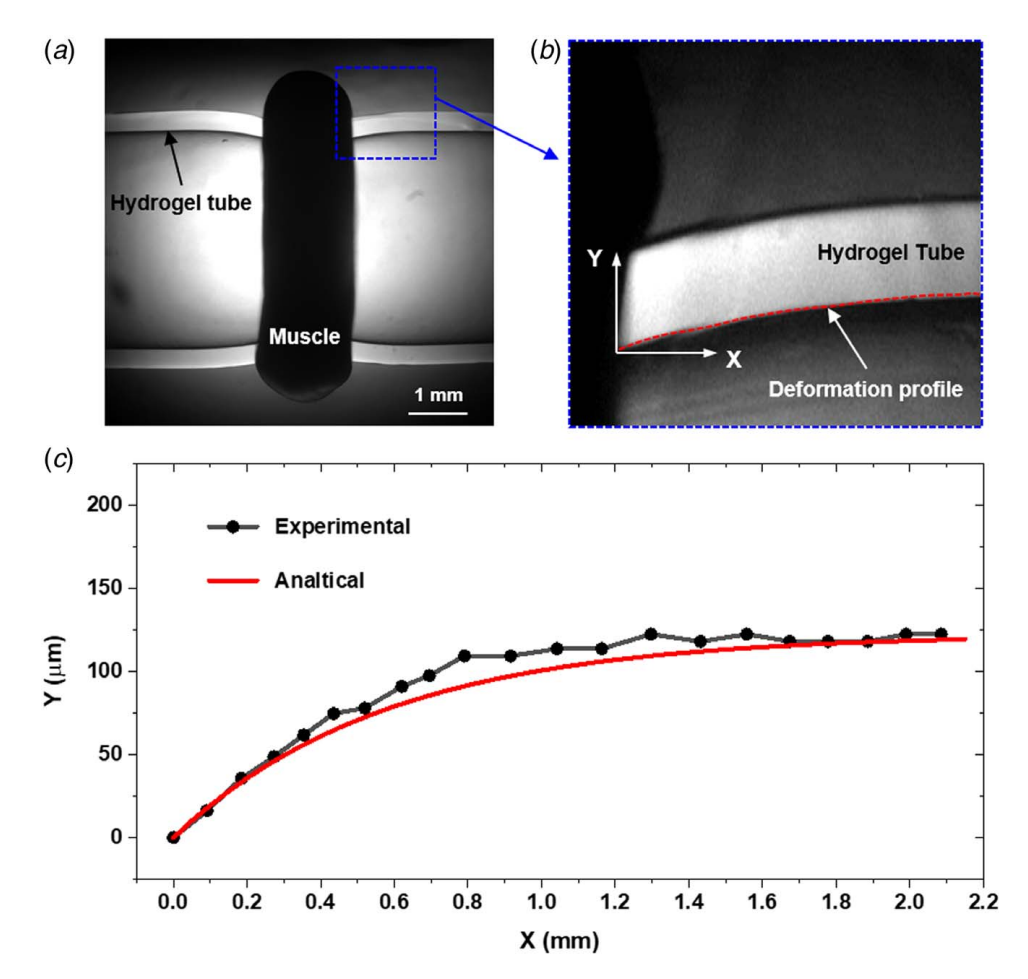


Fig. 3 (a) Phase-contrast image of a muscle ring wrapping around the hydrogel tube. (b) The magnified phase-contrast image marked in a dotted square shown in (a), where the image is enlarged 150% in the Y direction to more clearly show the deformation profile of hydrogel tube. (c) The comparison of the profile of deformed hydrogel tube between experimental measurements and analytical estimation by using the exponential equation  $y = y_0 e^{-x/x_0}$ , where  $x_0 = \sqrt{(Rt)/2} = 0.578$  mm.

Figure 3(a) gives one example of a prepared pump-bot in the experiment where the hydrogel tube is compressed under the static muscle contraction. Here, the tube thickness t is 0.336 mm, tube radius R is 1.992 mm (at the mid thickness), and the tube radius decreases near the muscle ring  $y_0$  to 120.18  $\mu$ m. The deformation profile of the tube is indicated in Fig. 3(b), where the image is elongated by 50% in the height direction for clarity. The deformation profile is reasonably approximated by an exponential function,  $y = y_0 e^{-x/x_0}$ , with  $x_0 = \sqrt{Rt/2} = 0.578$  mm (Fig. 3(c)), justifying the assumption of the model.

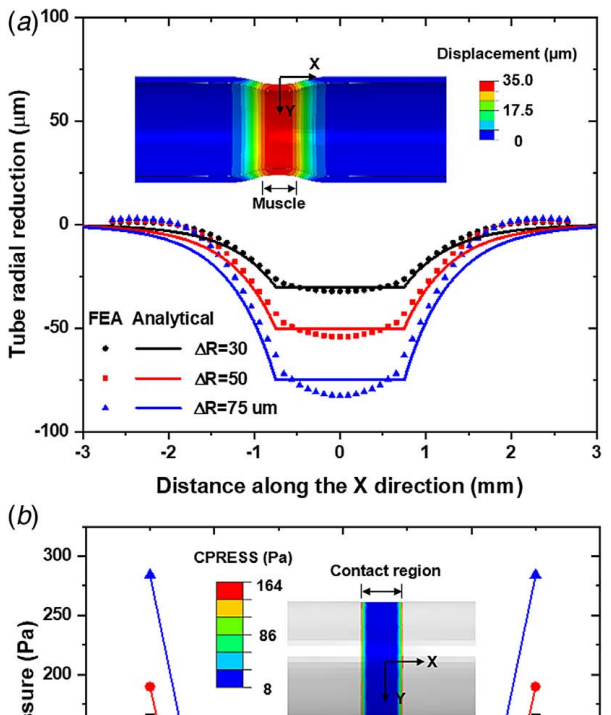
**2.3 Finite Element Analysis.** A full three-dimensional finite element model is performed to simulate the static muscle contraction observed in the experimental hydrogel tube with outer diameter 4.55 mm, length 30 mm, and wall thickness 0.275 mm. The muscle ring dimensions are outer diameter 5.05 mm, width 1.5 mm, and thickness 0.5 mm. Linear elastic model is used to describe the material behaviors of both hydrogel tube and muscle ring with Young's modulus and Poisson's ratio of  $E_t = 10$  kPa and  $\nu_t = 0.48$  [16] for hydrogel, and  $E_m = 15$  kPa and  $\nu_m = 0.48$  for the muscle. Eightnode, 3D solid elements (Abaqus element C3D8) are used to discretize the geometry. The interaction between muscle ring and hydrogel tube is considered to be "hard" contact without the penetration in the radial direction. Sliding is allowed along the tangential direction between the muscle and the tube without any frictional resistance. Circumferential contraction of the muscle ring is

simulated as "thermal shrinkage" by reducing temperature to deform the hydrogel tube.

Muscle contraction along the circumferential direction induces the radial compressive force on the hydrogel tube. The deformation profiles along the X direction obtained by finite element analysis (FEA) under different muscle contractions show good comparisons with the exponential shape based on the equation  $y = y_0 e^{-x/x_0}$  (Fig. 4(a)), where the inset shows the deformation of the hydrogel tube under 30  $\mu$ m radial reduction near the muscle ring. The distributions of the radial contact pressure on the tube caused by the static muscle contraction are shown in Fig. 4(b). The contact pressure near the edge of the contact region between muscle and tube are much higher than that in the middle region. A linear relationship between muscle tension and tube radius change is obtained, which agrees well with the analytical solutions given by Eq. (9) (Fig. 5).

## 3 Buckling and Postbuckling Analysis

**3.1 Experimental Observation.** In the experiment, we observed two typical configurations of the soft hydrogel tubes under the muscle contraction, i.e., unbuckled and buckled state. Figure 6(a) shows a side view of an unbuckled pump-bot tube. The tube does not show any folding or crease. The outer diameter and wall thickness of the hydrogel tube are 4.49 and 0.39 mm, respectively. The dimeter reduces by about  $52 \mu m$  due to static contraction of the muscle ring with thickness about 1.85 mm.



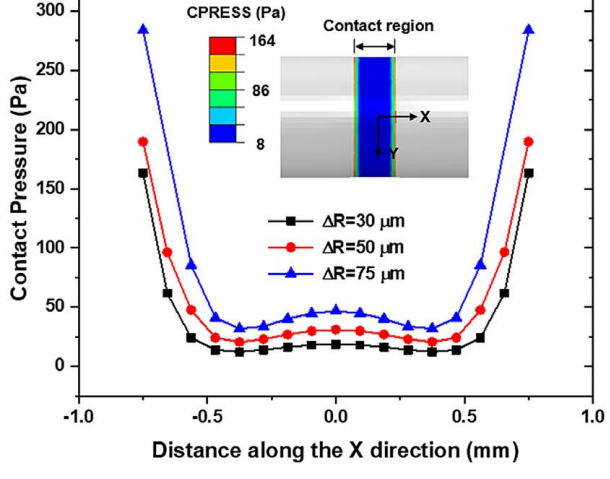


Fig. 4 (a) The comparisons of the deformation profile of deformed hydrogel tube obtained by FEA and analytical equation  $y=y_0e^{-x/x_0}$  under different muscle contraction amounts, where the inset shows the displacement contour of the hydrogel tube with  $30\,\mu\mathrm{m}$  radial reduction. (b) Distributions of the contact pressure along the contact region in the X direction on the hydrogel tube under different muscle contraction amounts.

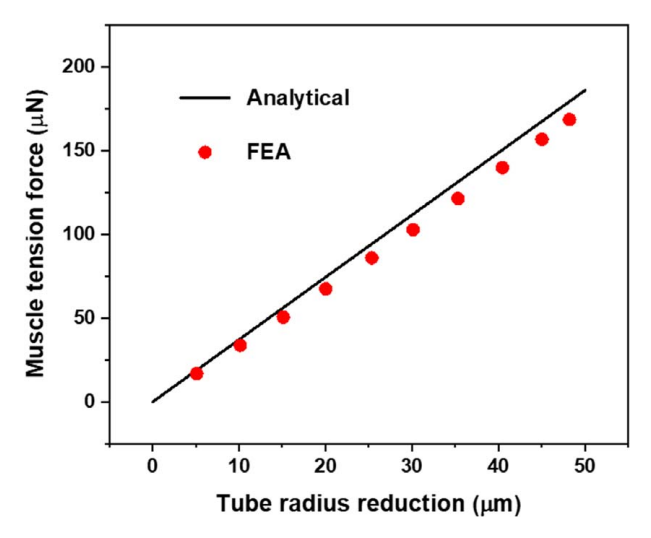


Fig. 5 Static muscle tension force as a function of tube radial reduction obtained from the analytical solution (line) which agrees well with FEA results (dots)

Figure 6(b) shows the cross-sectional image of an unbuckled tube. Here, we mounted the tube vertically using a 1 mm-diameter glass rod to take a cross-sectional image of the muscle ring/hydrogel tube.

However, we observe that some pump-bot show significant reduction in diameter and crease of the hydrogel tube when imaged transversely. Figure 6(c) shows a soft tube with 4.20 mm outer diameter. It reduces to about 3.50 mm due to muscle contraction. There is a much larger diameter reduction compared with the unbuckling case. The tube is thus expected to be buckled. Figure 6(d) shows that such a creased tube indeed buckles. Note that the muscles in Figs. 6(a)–6(d) are nominally similar, i.e., they are expected to produce similar static force. And yet, they may or may not cause the tube to buckle. To understand the origin of this discrepancy, we develop a model to predict buckling of elastic tubes subjected to the compression of a tensile ring (like a taut rubber band).

**3.2 Buckling Analysis.** The muscle shrinks over time after transferring to the hydrogel tube. This induces static compressive force on the tube, while the muscle is under the tension, T. To examine whether this tension can buckle the hydrogel tube, an analytical buckling analysis is performed. For simplicity, we consider the length of the tube is w, which is also the width of the muscle. First, we assume that the hydrogel tube is bucked under the muscle tension T, with the length of buckled arc T and amplitude T (Fig. T (T (T )). Both T and T are unknowns. We assume negligible tangential strain of the tube, i.e., the length of perimeter of the tube is constant. Let T T define the shape in the segment BC (Fig. T (T ) of the tube, where T is the coordinate along the perimeter:

$$y = \frac{D}{2} [1 - \cos(2\pi s/L)] \tag{10}$$

The change of curvature in BC is given by

$$\Delta \kappa = y''(s) - \frac{1}{R} \tag{11}$$

where R is the initial radius at the mid thickness of hydrogel tube. Therefore, the total strain energy in BC is

$$E_{BC} = \int \frac{M\Delta\kappa}{2} ds = \int_0^L \frac{(\Delta\kappa)^2 EI}{2} ds$$
 (12)

Substitute Eqs. (10) and (11) into Eq. (12), to obtain the strain energy in BC as

$$E_{BC} = \frac{EI}{2} \left[ \frac{D^2}{8} \left( \frac{2\pi}{L} \right)^4 L + \frac{L}{R^2} \right]$$
 (13)

The slope, y'(B) = 0, and curvature, y''(B), are continuous at B from AB to BC. The curvature of AB changes from 1/R to y''(B) due to the moment applied by BC at B. We assume that the moment at B on the segment AB is the only moment causing the change of curvature. Thus, the moment and hence the change of curvature are constant along AB (Fig. 7(c)). The change of angle from A to B is  $\pi/2$  over a distance( $\pi R - L$ )/2. Thus, the constant curvature along AB is  $\pi/(\pi R - L)$ . Continuity of curvature at B from AB to BC, together with Eq. (12) gives

$$y''|_{B} = \frac{D}{2} \left(\frac{2\pi}{L}\right)^{2} = \frac{\pi}{\pi R - L}$$
 (14)

Therefore, the relationship between D and L can be found as

$$D = \frac{L^2}{2\pi(\pi R - L)} \tag{15}$$

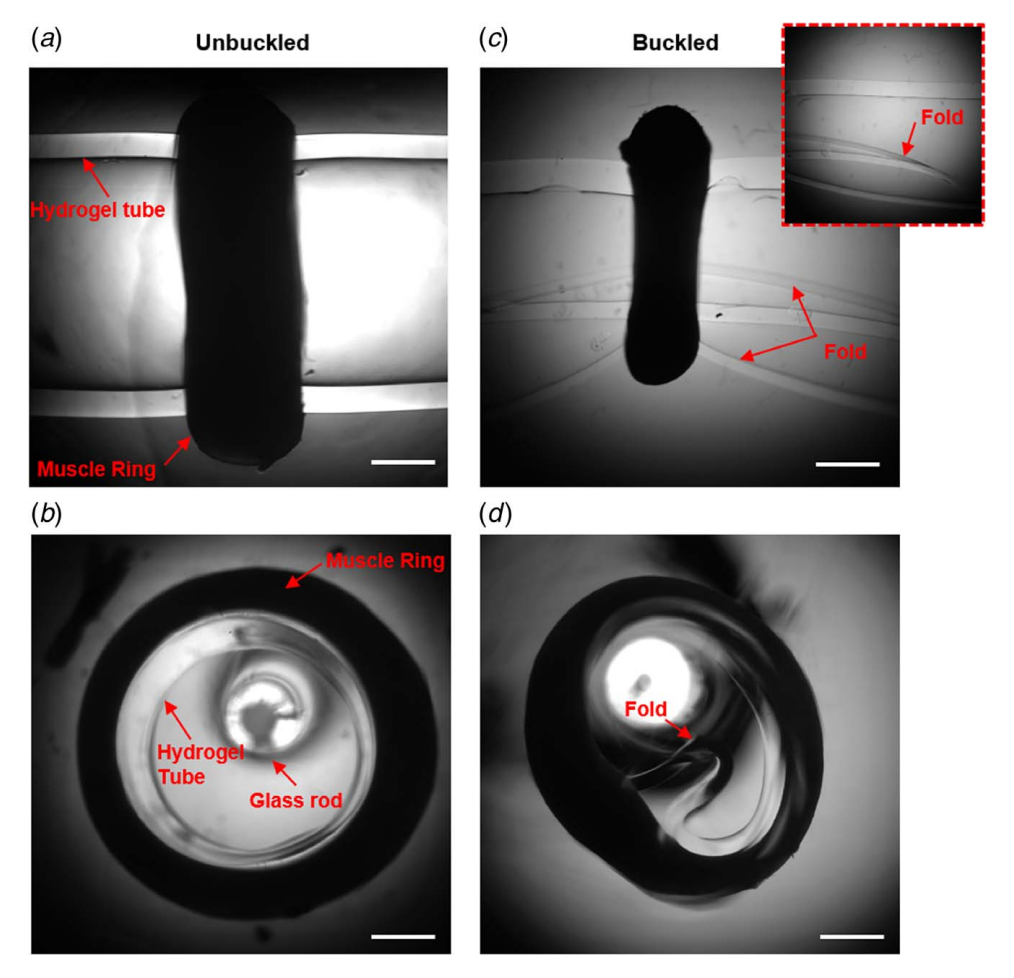


Fig. 6 Two typical configurations of the hydrogel tube observed in the experiment under the static muscle contraction. Phase-contrast image of a muscle ring wrapping around an unbuckled hydrogel tube from the (a) transverse view and (b) cross-sectional view [16]. Phase-contrast image of a muscle ring wrapping around a buckled hydrogel tube from the (a) transverse view and (b) cross-sectional view [16]. (Scale bar: 1 mm).

The change of curvature along AB is given by y - 1/R, so the strain energy in AB can be expressed as

$$E_{AB} = \frac{EI}{2} \int_{0}^{(\pi R - L)/2} \left( y'' - \frac{1}{R} \right)^{2} ds$$
 (16)

AB and CD in have the same strain energy

$$E_{AB+CD} = \frac{EI}{2} \left[ \frac{D}{2} \left( \frac{2\pi}{L} \right)^2 - \frac{1}{R} \right]^2 (\pi R - L) \tag{17}$$

Total strain energy from AB, BC, and CD can be expressed as

$$U = \frac{EI}{2} \left[ \left[ \frac{D}{2} \left( \frac{2\pi}{L} \right)^2 - \frac{1}{R} \right]^2 (\pi R - L) + \frac{D^2}{8} \left( \frac{2\pi}{L} \right)^4 + \frac{L}{R^2} \right]$$
(18)

The shortening of muscle ring  $\delta$  due to buckling is given by

$$\delta = L - \int_{0}^{L} \sqrt{1 - y^{2}} ds = \frac{\pi^{2} D^{2}}{4L}$$
 (19)

Let the muscle relax with shortening as  $T = T_0(1 - \delta/\delta_0)$ , where  $\delta_0$  is a constant. Then, the decrease in the potential energy of the muscle ring due to buckling of the tube is

$$W = \int T d\delta = \int_0^\delta T_0 \left( 1 - \frac{\delta}{\delta_0} \right) d\delta \tag{20}$$

Using Eq. (19)

$$W = T_0 \left[ \frac{\pi^2 D^2}{4L} - \frac{1}{2\delta_0} \left( \frac{\pi^2 D^2}{4L} \right)^2 \right]$$
 (21)

The total change in energy can be expressed as

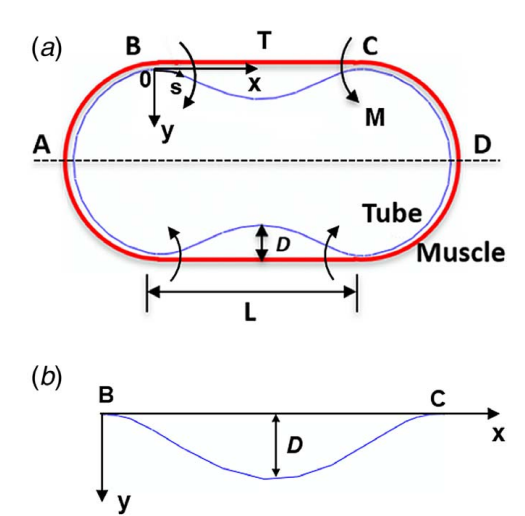
$$E_f = U - W \tag{22}$$

giving

$$E_f = \frac{\pi RT}{16} \left[ 4\lambda x (3 - 2x) - x^3 + \frac{1}{32\xi} \frac{x^6}{(1 - x)^2} \right] \frac{1}{(1 - x)^2}$$
 (23)

Where  $\lambda = EI/R^2T$ ,  $x = L/\pi R$ , and  $\xi = \delta_0/\pi R$  are the contraction ratio of the muscle ring and the tensile strain, respectively, before the tube is buckled.

Here,  $\lambda$  accounts for the material properties and the geometry of the tube, and the tension in the muscle before buckling. The nondimensional parameter,  $x \sim (0, 1)$ , L/gives a measure of buckling. When x = 0 (i.e., L = 0), there is no buckling, when x = 1 (i.e.,  $L = \pi R$ ), the entire perimeter of the tube is buckled. Equation (19) gives the energy landscape in  $x \sim (0, 1)$  to estimate the onset of buckling, or more importantly, the possible buckled states as a function of  $\lambda$  or T. Second derivative of  $E_f$  with respective tox, i.e.,  $d^2 E_f / dx^2$  gives the "stiffness" or the muscle-tube system. Onset of buckling from unbuckled state requires  $d^2 E_f / dx^2$  changing sign from positive to negative at x = 0 as T increases. At impending



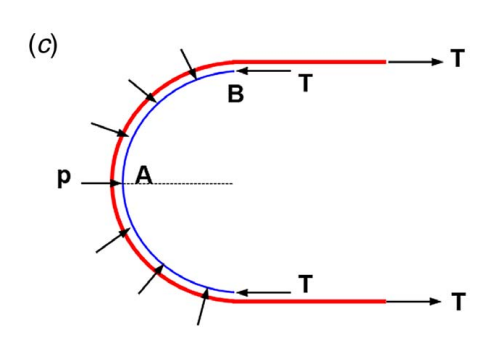


Fig. 7 (a) Buckling of hydrogel tube under the muscle tension. Free body diagrams of the (b) buckled segment BC and (c) unbuckled segment AB.

buckling  $d^2E_f/dx^2 = 0$ . However, we find  $d^2E_f/dx^2 = 32\lambda > 0$  at x = 0 for all  $\lambda > 0$ . This implies that the tube does not buckle for any finite T irrespective of  $\xi$ .

However, the energy landscape (plot of  $E_f$  versus x, Fig. 8) for various  $\lambda$  shows the appearance of a minimum at  $x_b > 0$  as  $\lambda$  decreases (i.e., T increases). This minimum represents a buckled state. But there is an energy barrier between the energy at x=0 and  $x_b$ . This implies that an unbuckled tube cannot be buckled by simply increasing muscle tension, but if the tube is first folded and then the muscle ring is applied with high enough tension, then it will reach the buckled state and the tube cannot unfold. This can be easily verified by a desktop experiment with taut rubber bands wrapping a soft tube. Two states of such a tube are

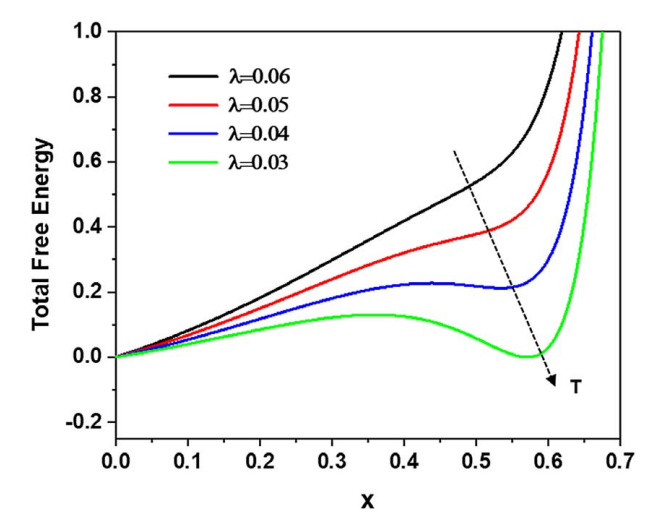


Fig. 8 The energy landscape of the biohybrid pumping system under various static muscle contraction forces, where  $\lambda = EI/R^2T$  and  $\mathbf{x} = L/\pi R$ 

shown in Fig. 9, buckled and unbuckled. The buckled state is arrived by first bending the tube and then wrapping with a taut band. The tube does not buckle spontaneously with increasing force of the rubber band wrapping around the circular tube. The force of the rubber band is much higher in the unbuckled state compared with that of the buckled one.

In the experiment with hydrogel tubes for pump-bots, we observe both buckled and unbuckled states. One possible explanation might be that the soft tube gets bent during the manual assembly of the muscle ring on the tube. If so, then the tube remains at a buckled state even with low muscle force. The pump still operates when the muscle contracts cyclically squeezing the buckled tube. Alternatively, the muscle rings may not be perfectly uniform along the circumferential direction. The nature and the origin of this possible nonuniformity is not known and hence was not considered in the model. An obvious nonuniformity is the variation in thickness of the muscle ring along the circumferential direction, some segments are thicker than others (Fig. 6(d)). The thicker segment will push the tube radially inward and bend it locally, leading to the buckling of the tube as the muscle force increases with time. Irrespective of the state of the tube under muscle force, buckled or unbuckled, cyclic contraction of the muscle ring results in pumping of fluid for the impedance pump, although the pumping rate and efficiency will depend on the state. This robustness of impedance pumps might be the reason for its choice for circulation in early developmental stage.





Fig. 9 A desktop experiment demonstrating experiment with a compliant tube and a taut rubber band wrapping a tube. (a) No buckling occurred under high tension of rubber band on the circular tube. (b) Buckled state of the tube achieved by pre-bending the tube and then applying the rubber band. Here, tension of the band is less than that in (a).

#### 4 Conclusion

This work was motivated by the design and development of a biohybrid impedance pump (valveless) where pumping is achieved by a muscle ring squeezing a soft hydrogel tube. Experiments show that the contractile force of the muscle ring occasionally buckles the tube in a random and unpredictable fashion. In order to explain this anomaly, we developed an analytical model to predict the deformation and stability of an elastic tube subjected to a contractile band squeezing the tube. The model predictions are validated by experimental measurements and finite element analysis. Buckling and postbuckling analysis using the model reveals that elastic tubes may not buckle even under large muscle contractile force unless the tube is first bent locally and then the muscle ring is applied. This can happen during assembly of the muscle ring on the tube, or by nonuniform geometry of the muscle ring where thicker region of the muscle bending the tube locally. This insight from the model explains the apparent anomalous experimental observation of inconsistent buckling of hydrogel tubes of the pump. The analysis will guide the design of more complex, high-performance biohybrid pump-bots and systems by harnessing the structural buckling to achieve higher net flow.

#### Acknowledgment

This work is funded by the National Science Foundation (NSF), Science and Technology Center on Emergent Behaviors in Integrated Cellular Systems (EBICS) Grant CBET-0939511, and NSF Emerging Frontiers in Research and Innovation (EFRI): Continuum, Compliant, and Configurable Soft Robotics Engineering (C3 SoRo) Grant 1830881.

#### **Conflict of Interest**

There are no conflicts of interest.

## **Data Availability Statement**

The datasets generated and supporting the findings of this article are obtainable from the corresponding author upon reasonable request. The authors attest that all data for this study are included in the paper.

### References

[1] Feinberg, A. W., Feigel, A., Shevkoplyas, S. S., Sheehy, S., Whitesides, G. M., and Parker, K. K., 2007, "Muscular Thin Films for Building Actuators and Powering Devices," Science, 317(5843), pp. 1366–1370.

- [2] Ricotti, L., Trimmer, B., Feinberg, A. W., Raman, R., Parker, K. K., Bashir, R., Sitti, M., Martel, S., Dario, P., and Menciassi, A., 2017, "Biohybrid Actuators for Robotics: A Review of Devices Actuated by Living Cells," Sci. Rob., 2(12), p. eaaq0495.
- [3] Kamm, R. D., and Bashir, R., 2014, "Creating Living Cellular Machines," Ann. Biomed. Eng., 42(2), pp. 445–459.
- [4] Patino, T., Mestre, R., and Sanchez, S., 2016, "Miniaturized Soft Bio-Hybrid Robotics: A Step Forward Into Healthcare Applications," Lab Chip, 16(19), pp. 3626–3630.
- [5] Sun, L., Yu, Y., Chen, Z., Bian, F., Ye, F., Sun, L., and Zhao, Y., 2020, "Biohybrid Robotics With Living Cell Actuation," Chem. Soc. Rev., 49(12), pp. 4043–4069.
- [6] Raman, R., Cvetkovic, C., and Bashir, R., 2017, "A Modular Approach to the Design, Fabrication, and Characterization of Muscle-Powered Biological Machines," Nat. Protoc., 12(3), pp. 519–533.
- [7] Raman, R., Cvetkovic, C., Uzel, S. G., Platt, R. J., Sengupta, P., Kamm, R. D., and Bashir, R., 2016, "Optogenetic Skeletal Muscle-Powered Adaptive Biological Machines," Proc. Natl. Acad. Sci. USA, 113(13), pp. 3497–3502.
- [8] Chan, V., Park, K., Collens, M. B., Kong, H., Saif, T. A., and Bashir, R., 2012, "Development of Miniaturized Walking Biological Machines," Sci. Rep., 2(1), pp. 1–8.
- [9] Cvetkovic, C., Raman, R., Chan, V., Williams, B. J., Tolish, M., Bajaj, P., Sakar, M. S., Asada, H. H., Saif, M. T. A., and Bashir, R., 2014, "Three-Dimensionally Printed Biological Machines Powered by Skeletal Muscle," Proc. Natl. Acad. Sci. USA, 111(28), pp. 10125–10130.
- [10] Park, S. J., Gazzola, M., Park, K. S., Park, S., Di Santo, V., Blevins, E. L., Lind, J. U., Campbell, P. H., Dauth, S., Capulli, A. K., and Pasqualini, F. S., 2016, "Phototactic Guidance of a Tissue-Engineered Soft-Robotic Ray," Science, 353(6295), pp. 158–162.
- [11] Williams, B. J., Anand, S. V., Rajagopalan, J., and Saif, M. T. A., 2014, "A Self-Propelled Biohybrid Swimmer at Low Reynolds Number," Nat. Commun., 5(1), pp. 1–8.
- [12] Nawroth, J. C., Lee, H., Feinberg, A. W., Ripplinger, C. M., McCain, M. L., Grosberg, A., Dabiri, J. O., and Parker, K. K., 2012, "A Tissue-Engineered Jellyfish With Biomimetic Propulsion," Nat. Biotechnol., 30(8), pp. 792–797.
- [13] Morimoto, Y., Onoe, H., and Takeuchi, S., 2018, "Biohybrid Robot Powered by an Antagonistic Pair of Skeletal Muscle Tissues," Sci. Rob., 3(18), p. eaat4440.
- [14] Akiyama, Y., Sakuma, T., Funakoshi, K., Hoshino, T., Iwabuchi, K., and Morishima, K., 2013, "Atmospheric-Operable Bioactuator Powered by Insect Muscle Packaged With Medium," Lab Chip, 13(24), pp. 4870–4880.
- [15] Justus, K. B., Hellebrekers, T., Lewis, D. D., Wood, A., Ingham, C., Majidi, C., LeDuc, P. R., and Tan, C., 2019, "A Biosensing Soft Robot: Autonomous Parsing of Chemical Signals Through Integrated Organic and Inorganic Interfaces," Sci Rob., 4(31), p. eaax0765.
- [16] Li, Z., Seo, Y., Aydin, O., Elhebeary, M., Kamm, R. D., Kong, H., and Saif, M. T. A., 2019, "Biohybrid Valveless Pump-Bot Powered by Engineered Skeletal Muscle," Proc. Natl. Acad. Sci. USA, 116(5), pp. 1543–1548.
- [17] Tanaka, Y., Morishima, K., Shimizu, T., Kikuchi, A., Yamato, M., Okano, T., and Kitamori, T., 2006, "An Actuated Pump on-Chip Powered by Cultured Cardiomyocytes," Lab Chip, 6(3), pp. 362–368.
- [18] Park, J., Kim, I. C., Baek, J., Cha, M., Kim, J., Park, S., Lee, J., and Kim, B., 2007, "Micro Pumping With Cardiomyocyte–Polymer Hybrid," Lab Chip, 7(10), pp. 1367–1370.
- [19] Li, Z., Tofangchi, A., Stavins, R. A., Emon, B., McKinney, R. D., Grippo, P. J., and Saif, M. T. A., 2021, "A Portable Pen-Sized Instrumentation to Measure Stiffness of Soft Tissues in Vivo," Sci. Rep., 11(1), pp. 1–11.
- [20] Li, Z., and Xiao, J., 2015, "Mechanics and Optics of Stretchable Elastomeric Microlens Array for Artificial Compound Eye Camera," J. Appl. Phys., 117(1), p. 014904.